Research Article Vol. 33, No. 2 / 27 Jan 2025 / Optics Express 2529
Optics EXPRESS

Growth, structure, spectroscopic, and laser properties of Ho-doped yttrium gallium garnet crystal

Sami Slimi,[1,2] Haohai Yu,[3] Huaijin Zhang,[3] Christian Kränkel,[4] Pavel Loiko,[5] Rosa Maria Solé,[2] Magdalena Aguiló,[2] Francesc Díaz,[2] Weidong Chen,[1,6] Uwe Griebner,[1] Valentin Petrov,[1] and Xavier Mateos[2,†,*]

[1]*Max Born Institute for Nonlinear Optics and Short Pulse Spectroscopy, Max-Born-Str. 2a, 12489 Berlin, Germany*
[2]*Universitat Rovira i Virgili (URV), Física i Cristal·lografia de Materials (FiCMA), Marcel.li Domingo 1, 43007 Tarragona, Spain*
[3]*State Key Laboratory of Crystal Materials, Shandong University, Jinan 250100, China*
[4]*Leibniz-Institut für Kristallzüchtung (IKZ), Max-Born-Str. 2, 12489 Berlin, Germany*
[5]*Centre de Recherche sur les Ions, les Matériaux et la Photonique (CIMAP), UMR 6252 CEA-CNRS-ENSICAEN, Université de Caen, 6 Boulevard Maréchal Juin, 14050 Caen Cedex 4, France*
[6]*Fujian Institute of Research on the Structure of Matter, Chinese Academy of Sciences, 350002 Fuzhou, China*
[†]Serra Húnter Fellow
[*]*xavier.mateos@urv.cat*

Abstract: We report on the growth of a 2.86 at.% Ho:YGG crystal using the optical floating zone technique in an oxygen-rich environment, followed by the study of its structure, optical spectroscopy and first demonstration of continuous-wave laser operation at 2.1 μm. The crystal structure refined through the Rietveld method reaffirms the cubic symmetry (sp. gr. $Ia\bar{3}d$, $a = 12.2796(9)$ Å). The absorption, stimulated-emission (SE), and gain cross-sections for the $^5I_8 \leftrightarrow {}^5I_7$ Ho^{3+} transition were determined from the spectroscopic studies. The SE cross-section, σ_{SE}, amounts to 9.5×10^{-21} cm^2 at 2084 nm, and the luminescence lifetime of the $^5I_7$ state is 8.94 ms. Among the Ho-doped garnets, Ho:YGG is characterized by smoother gain cross sections and a long luminescence lifetime. Laser operation of the Ho:YGG crystal is showcased using a 1908 nm Tm-fiber laser as a pump source. The in-band pumped Ho:YGG laser delivers 976 mW at 2085 and 2109 nm with a slope efficiency of 50.1%.

© 2025 Optica Publishing Group under the terms of the Optica Open Access Publishing Agreement

1. Introduction

Solid-state lasers operating around 2 μm ("eye-safe" radiation) find numerous applications in range-finding, remote sensing and wind mapping (LIDAR) [1,2], spectroscopy of molecular species, material processing, and frequency down-conversion to the mid-infrared via pumping optical parametric oscillators / amplifiers based on non-oxide nonlinear crystals [3–5]. Laser action in this spectral range can be attained using Tm^{3+} and Ho^{3+} activator ions. Holmium ions (Ho^{3+}, electronic configuration: $[Xe]4f^{10}$), enable emission slightly above 2 μm owing to their $^5I_7 \rightarrow {}^5I_8$ electronic transition. This helps to avoid the spectral overlap with the intense absorption lines of water vapors in the atmosphere being essential for generation of femtosecond pulses from mode-locked lasers [6–8].

All-solid-state lasers based on Ho^{3+}-doped materials rely on the so-called in-band resonant pumping scheme (i.e., excitation directly to the upper laser level, $^5I_7$) [9,10]. It naturally provides high laser efficiency and relatively weak heat loading [11]. Still, due to the energy-transfer

#540363 https://doi.org/10.1364/OE.540363
Journal © 2025 Received 30 Aug 2024; revised 20 Nov 2024; accepted 8 Dec 2024; published 17 Jan 2025

Optics EXPRESS

upconversion (ETU) from the metastable manifold, $^5I_7 + {}^5I_7 \rightarrow {}^5I_6 + {}^5I_8$, this scheme requires optimization of the Ho^{3+} doping level [12]. It is well known that high concentrations of Ho^{3+} dopant ions lead to a considerable increase in upconversion losses, which degrade the performance of 2-μm lasers based on this ion. High doping levels contribute to significant heat loading in the gain medium, and the ETU process amplifies these thermal effects, raising cavity losses and crystal temperature. This increase in temperature and losses subsequently leads to a higher lasing threshold and a greater excitation density in the upper energy manifold, which further accelerates the ETU rate. These cascading effects in heavily Ho^{3+}-doped samples can cause a marked decrease in both the output power and laser efficiency and usually a few at.% of Ho^{3+} ions is recommended to avoid such effects [13].

In-band pumping of Ho-lasers has been readily achieved by commercially available Tm-fiber lasers or GaSb-based laser diodes emitting around 1.9-1.95 μm.

Among the laser crystals employed for doping with Ho^{3+} ions for 2-μm emission, cubic garnets such as the yttrium aluminium garnet, $Y_3Al_5O_{12}$ (shortly YAG), are widely used. As a host crystal, YAG offers good thermal and thermo-mechanical properties and easy accommodation of rare-earth ions. The dopant Ho^{3+} ions in YAG feature a relatively large Stark splitting of the ground-state ($^5I_8$, ~540 cm^{-1}) and a long luminescence lifetime of the upper laser level ($^5I_7$, ~7 ms) [14]. The main drawback of Ho:YAG as a gain medium for 2-μm lasers is its relatively narrow gain bandwidth at 2.1 μm. Efficient [15] and power-scalable bulk [16,17] and thin-disk [18] 2.1-μm Ho:YAG lasers operating in the continuous-wave and mode-locked regimes have been reported. The optimization of the Ho^{3+} doping level for such lasers is still a challenge as it represents a compromise between boosting the pump absorption efficiency and limiting the reduction of the thermal conductivity, as well as maintaining relatively weak ETU [19]. Garnet crystals with high segregation coefficient for Ho^{3+} doping and at the same time enabling efficient in-band pumped laser operation are in high demand, e.g., for thin-disk lasers.

Within the family of cubic garnets, gallium compounds attract a lot of attention for solid-state laser engineering due to a combination of appealing thermal and spectroscopic properties [20]. One example is the yttrium gallium garnet ($Y_3Ga_5O_{12}$, YGG) [21]. Apart from its high thermal conductivity and easy doping with rare-earth ions, this crystal features a lower maximum phonon energy ($h\nu_{ph}$ ~783 cm^{-1}) as compared to YAG ($h\nu_{ph}$ ~857 cm^{-1}), reducing the probability of multiphonon non-radiative relaxation, which is relevant for the $^5I_7$ Ho^{3+} manifold. It is usually grown by the optical floating zone method or Czochralski technique. The spectroscopic properties and laser operation of YGG crystals doped with Yb^{3+} [20,21], Tm^{3+} [22], and Er^{3+} [23] ions have been studied previously. The optical properties including the absorption and emission spectra, and the determination of energy levels of the $^5I_8$ ground state and $^5I_7$ excited state of Ho^{3+} ions in YGG host was previously reported by G. J. Dixon and L. F. Johnson [24]. There are only two reports on laser action on the $^5I_7 \rightarrow {}^5I_8$ Ho^{3+} transition in the YGG crystal, the first concerns the Tm^{3+},Ho^{3+} codoping scheme with ~0.8 μm pumping: a diode-pumped Tm,Ho:YGG laser delivered 1.33 W at 2086nm albeit with a low efficiency of 10.8% [25]. And the second operation was conducted at cryogenic temperature at 77 K using Fe, Ho:YGG codoped where the pumping into the Ho^{3+} bands at 1.2 μm was provided by nonradiative energy transfer from Fe^{3+} ions excited at 0.9-1 μm [26].

In the present work, we report on the crystal growth, spectroscopy and in-band pumped laser operation of a Ho^{3+}-doped YGG crystal with the goal of developing novel materials for power-scalable and ultrashort pulse lasers at ~2 μm.

2. Crystal growth and structure

2.1. Crystal growth

The Ho:YGG crystal was grown by the optical floating zone (OFZ) method under an oxygen-rich atmosphere. The raw materials were oxide powders of Ho_2O_3 (Alfa Aesar, purity: 4N), Y_2O_3

Optics EXPRESS

(Alfa Aesar, 4N), and Ga_2O_3 (Macklin, 4N). These raw materials were accurately weighed in the stoichiometric ratios with the doping concentration (x) of Ho^{3+} ions of 2.5 at.% (with respect to Y^{3+}) in YGG, and then mixed in ethanol. After drying and grinding, the as-obtained mixture was calcined in a muffle furnace at a temperature of 1000 °C for 5 hours following the solid-state reaction:

$$x\mathrm{Ho_2O_3} + (3\text{-}x)\mathrm{Y_2O_3} + 5\mathrm{Ga_2O_3} \rightarrow 2(\mathrm{Ho}_x\mathrm{Y}_{3-x})\mathrm{Ga_5O_{12}}.$$

Subsequently, the sintered powder was ground again and then used to prepare the seed and feed rods, which needed to be pressed under 60 MPa for 10 minutes. The obtained rods were sintered at 1300 °C in air for 5 hours. The sample was moved to a four-ellipsoidal-mirror OFZ furnace (Crystal Systems Inc., FZ-T-12000-X-I-S-SU) where it was exposed to four xenon lamps. The growth parameters were optimized as follows: the rotation rates of the feed and seed rods were set at 15 rpm (revolutions per minute), and the growth rate was fixed at 6 mm/hour. Moreover, to reduce the volatilization of the gallium component, the growth atmosphere was under pure O_2 with a flow rate of 250 ml/min. Finally, when the growth process was finished, the furnace was slowly cooled down to room temperature (RT) within 3.5 hours. No annealing was applied.

A photograph of an as-grown Ho:YGG crystal is shown in Fig. 1. The boule had a cylindrical shape with length of 3.5 cm and a diameter of 5 mm, and it was free of cracks, inclusions, and bubbles. The actual concentration of Ho^{3+} ions within the crystal amounted to 2.86 at.%, as determined using the electron probe microanalysis (EPMA) technique. The corresponding Ho^{3+} ion density was calculated to be $N_{\mathrm{Ho}} = 3.69 \times 10^{20}$ at/cm^3 and the segregation coefficient for the dopant ions K_{Ho} was 1.14.

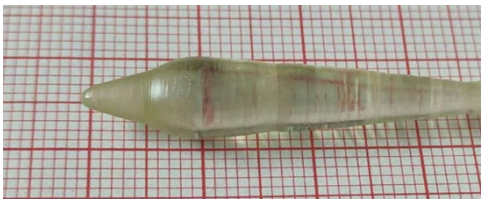

Fig. 1. Photograph of an as-grown 2.86 at.% Ho:YGG crystal (starting composition).

2.2. Structure refinement

X-ray powder diffraction (XRD) analysis was utilized to verify the phase purity and structure of the grown crystal. For this, we employed a Bruker-AXS D8-Advance diffractometer in a θ-θ Bragg Brentano configuration (Billerica, USA) with Cu Kα ($\lambda = 1.5406$ Å) radiation, and the measurements were conducted over a 2θ range of 5° to 80°, employing a step size of 0.02° and a step time of 16 s. The Rietveld refinement method was further applied. Figure 2 illustrates the refinement plot for the as-grown Ho:YGG crystal, featuring the observed, calculated, and residual patterns, as well as the Bragg positions. Table 1 presents the refinement parameters. The initial atomic coordinates for undoped YGG utilized for the structure refinement were taken from Ref. [27].

The Ho:YGG crystal adopts a typical cubic garnet structure with a general chemical formula $\{A\}_3[B]_2(C)_3O_{12}$ (space group $O^{10}{}_h$- $Ia\bar{3}d$, No.230, point group $m\bar{3}m$), where {A}, [B], and (C) stand for dodecahedral (Wyckoff: 24c), octahedral (16a), and tetrahedral (24d) sites, respectively [28]. For Ho:YGG, this formula reads $\{Y|Ho\}_3[Ga]_2(Ga)_3O_{12}$. Its lattice constant a is 12.2796(9) Å, the unit-cell volume V is 1851.123(0) Å^3, and the calculated crystal density ρ_{calc} is 5.944 g/cm^3 (with the number of formula units per unit-cell $Z = 8$), as determined through the Rietveld refinement. The reduced chi-squared value of $\chi^2 = (R_{wp}/R_{exp})^2$ for this sample is 4.72 ($R_{wp} = 11.1\%$, $R_{exp} = 5.10\%$) indicating that the fit has converged. The fractional atomic

Optics EXPRESS

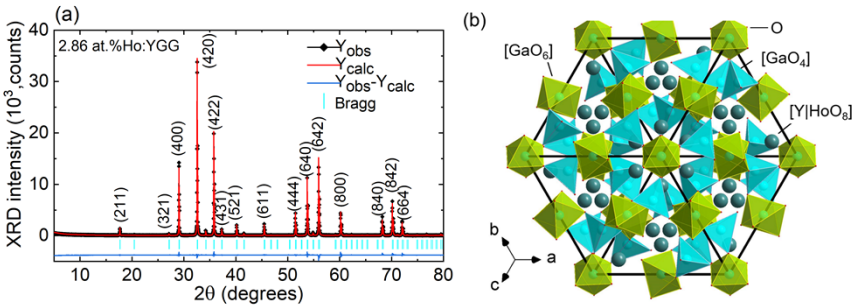

Fig. 2. The structure of 2.86 at.% Ho:YGG: (a) Rietveld structure refinement of the XRD pattern, depicting the measured (Y_{obs}, *black*), calculated (Y_{calc}, *red*), and residual (Y_{obs} – Y_{calc}, *blue*) patterns. *Cyan dashed lines* represent the Bragg reflections, with numbers denoting the Miller's indices (*hkl*); (b) a fragment of the crystal structure along the [111] axis.

Table 1. Parameters of the Rietveld structure refinement for 2.86 at.% Ho:YGG

Parameter	Value
Formula	$Y_{2.9142}Ho_{0.0858}Ga_5O_{12}$
Crystal system	cubic
Space group (IT number, Z)	$Ia\bar{3}d$ (230, 8)
Laue class	$m\bar{3}m$
Calculated density (g/cm^3)	5.944
Lattice constant $a = b = c$ (Å)	12.2796(9)
$\alpha = \beta = \gamma$ (deg.)	90
Volume (Å^3)	1851.123(0)
2θ range (deg.)	5-80
2θ step (deg.)	0.02
Radiation	Cu-Kα_1 ($\lambda = 1.5418$ Å)
No. of reflections	104
Refinement software	Match3! (Crystal impact) software
Reliability factors	R_p =8.03, R_{wp} = 11.1, R_{exp} = 5.10 and χ^2 = 4.72

coordinates (*x*, *y*, *z*), the site occupancy factors (O.F.), and isotropic displacement parameters (B_{iso}) for the Ho:YGG crystal are detailed in Table 2.

Table 2. Fractional atomic coordinates, site occupancy factors and isotropic displacement parameters for 2.86 at.% Ho:YGG

Atoms	Wyckoff	*x*/*a*	*y*/*b*	*z*/*c*	O.F.	B_{iso} (Å^2)
Y|Ho	24*c*	1/8	0	1/4	0.9714|0.0286	0.92(16)
Ga1	16*a*	0	0	0	1	1.827(0)
Ga2	24*d*	0.3750(0)	0	1/4	1	1.237(0)
O	96*h*	-0.0268(4)	0.0572(5)	0.1531(7)	1	2.170(0)

The dopant Ho^{3+} ions are expected to replace for the host-forming Y^{3+} cations due to the closeness of the corresponding ionic radii for VIII-fold oxygen coordination, $R_h(Y^{3+}) = 1.019$ Å and $R_d(Ho^{3+}) = 1.015$ Å. The corresponding percentage difference, $Dr = (R_h - R_d)/R_h \times 100\%$, is only 3.34%.

Optics EXPRESS

In Ho:YGG, the rare-earth (Y|Ho) atoms occupy the dodecahedral sites {A} coordinated by eight O atoms. There are three groups of interatomic distances Y|Ho – O, namely $2\times2.4165(5)$ Å, $4\times2.3219(7)$ Å, and $2\times2.4165(5)$ Å. The Ga^{3+} ions are distributed over two different sites within the crystal lattice: the octahedral [B] and tetrahedral (C) ones, surrounded by six and four oxygens, respectively. The [GaO_6] and [GaO_4] polyhedrons are interconnected by sharing the same O^{2-} ions. The bond lengths Ga – O in the [GaO_6] octahedrons are $6\times2.0364(2)$ Å, while inside the tetrahedrons [GaO_4], the Ga – O interatomic distances are $4\times1.8351(1)$ Å. The distortion index for the gallium polyhedrons is zero as all the metal – oxygen distances are equal.

2.3. Raman spectra

The Raman spectrum of the grown crystal was measured using a confocal Raman microscope (Renishaw InVia) equipped with a $\times50$ Leica objective, and a He-Ne laser as an excitation source ($\lambda = 633$ nm). The primitive unit cell of the cubic garnet lattice comprises four formula units (equivalent to 80 atoms). By means of the factor group analysis, a total of 25 Raman-active modes is determined, classified into $3A_1$ g, $8E_g$, and $14T_2$ g irreducible representations [29]. The Raman spectrum of Ho:YGG, cf. Figure 3, can be divided into two main regions: a low-frequency (100-300 cm^{-1}) and a high-frequency (300-800 cm^{-1}) one. In the latter range, bands associated with antisymmetric stretching vibrations of the [GaO_6] and [GaO_4] polyhedrons are observed at 400-580 cm^{-1} and 580-700 cm^{-1}, respectively. In particular, the band at 351 cm^{-1} is assigned to a symmetric stretching vibration of [GaO_4], coupled with a rotational movement encompassing the entire tetrahedron. The most intensive Raman line at 757 cm^{-1} primarily arises from the symmetric stretching mode of the [GaO_4] tetrahedron and this peak is overlapping with the one corresponding to the maximum phonon frequency of 783 cm^{-1}. In the low-frequency range, the bands primarily originate from the O-Ga-O bending modes of the gallium polyhedrons, alongside the lattice modes associated with the vibrations of these polyhedrons relative to the rare-earth ions. These vibrations can be comprehended as stretching or bending modes of the dodecahedrons [Y|HoO_8] with the highest phonon frequency at 783 cm^{-1}.

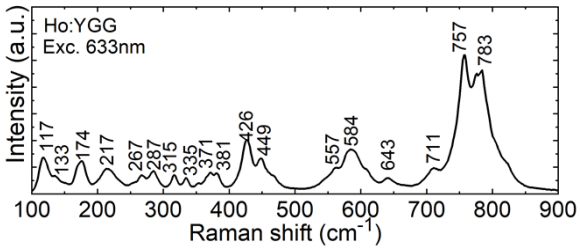

Fig. 3. Raman spectrum of 2.86 at.% Ho:YGG, *numbers* indicate the phonon energies in cm^{-1}, $\lambda_{exc} = 633$ nm.

2.4. Electronic structure

The band structure and the densities of states (DOS) of the garnet host YGG were calculated using the CASTEP code, employing a plane-wave pseudopotential total energy calculation method grounded in density functional theory (DFT). The electronic wave functions were extended using a plane-wave basis set with a self-consistent field (SCF) tolerance of 1×10^{-5} eV/Å. The non-conserving pseudopotentials and a $5\times5\times5$ k-point sampling were selected for the calculation. The calculated band structure and the total density of states (TDOS) of YGG, based on the refined crystal data, are presented in Fig. 4(a) and (b), respectively. Notably, both the bottom of the conduction band (CB) (3.49 eV) and the top of the valence band (VB) (0 eV - Fermi energy level) are at the same G point, meaning that YGG is a direct bandgap material

Optics EXPRESS

(E_g = 3.49 eV). In Fig. 4(c), the atom-resolved partial densities of states (PDOS) for Y, Ga and O are showcased. The conduction band is primarily determined by the d-state of Y and the s-state of Ga. Conversely, the valence band, stretching from the Fermi energy level located at 0 eV down to approximately -6.81 eV, is predominantly influenced by the 2p O and 3p, 3d Ga states.

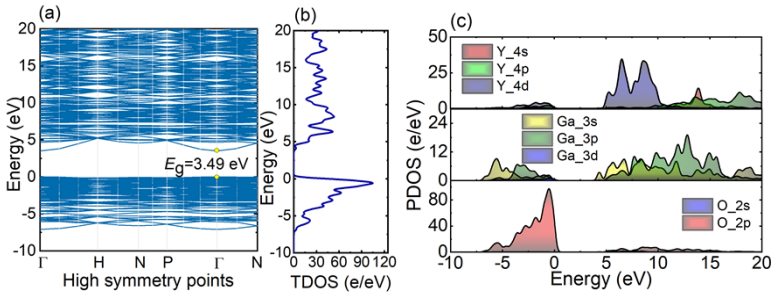

Fig. 4. Electronic structure of YGG crystal: (a) calculated band structure; (b) total density of states (TDOS); (c) Partial densities of states (PDOS) for Y, Ga and O.

3. Optical spectroscopy

3.1. Optical absorption

The spectroscopic properties of Ho:YGG were studied at RT. The transmission spectrum at 250–2200 nm was measured using a Varian CARY 5000 spectrophotometer. In the mid-infrared, a FTIR spectrometer (Jasco FI/IR 6700) was used.

The overview transmission spectrum is shown in Fig. 5. The sharp Ho^{3+} absorption lines are evident. These bands correspond to transitions from the ground state ($^5I_8$) to various excited states (ranging from $^5I_7$, at ~2 μm, to (^{5} G,^{3} H)$_5$ + $^3H_6$, at 0.36 μm). In the visible, there is a broad and faint absorption band spanning from 400 to 600 nm, which originates from color centers linked to cationic vacancies. The weak yellow-brown coloration of the as-grown crystal is a consequence of the combined effects of color center and Ho^{3+} absorption. The determination of the optical bandgap by the Tauc method is complicated by Ho^{3+} spectral bands in the UV spectral range, an estimate of $E_{g,opt}$ gives ~ 5 eV. In the mid-infrared, the crystal shows a broad transparency, with the IR absorption edge around 7.45 μm.

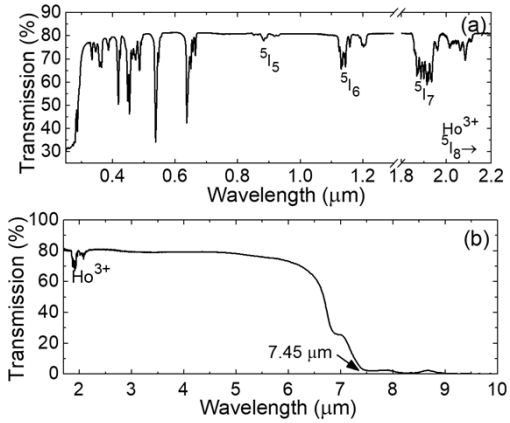

Fig. 5. Transmission spectrum of the as-grown Ho:YGG crystal: (a) visible and near-infrared ranges; (b) mid-infrared range. Sample thickness: 2.0 mm.

Optics EXPRESS

The Ho^{3+} absorption around 2 µm is due to the transition from the $^5I_8$ ground state to the lowest-lying excited state $^5I_7$ serving as the upper laser level, see Fig. 6. The absorption spectrum is relatively broad and structured due to the strong crystal-fields inherent to dodecahedral sites of garnets. Compared to the absorption spectrum of Ho:YAG, however, that of Ho:YGG is much less structured, as seen in Fig. 6. Next, the absorption cross-sections, $\sigma_{abs} = \alpha_{abs}/N_{Ho}$, were calculated, where α_{abs} is the absorption coefficient. The maximum σ_{abs} amounts to 0.37×10^{-20} cm^2 at 1914nm and the absorption bandwidth (full width at half-maximum, FWHM) is relatively large, about 7 nm. At the pump wavelength employed in the present work (1908nm), σ_{abs} is about 30% lower (0.26×10^{-20} cm^2). This pump transition can be addressed by GaSb diode lasers and Tm-fiber lasers resulting in resonant (in-band) pumping directly to the upper laser level.

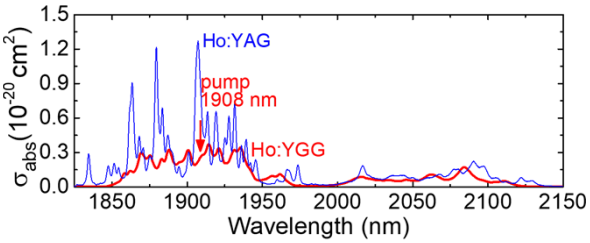

Fig. 6. Absorption cross-sections, σ_{abs}, of Ho^{3+} in YGG for the $^5I_8 \rightarrow {}^5I_7$ transition. The σ_{abs} spectrum for Ho:YAG is added for comparison.

3.2. *Emission (spectra and lifetime)*

The stimulated-emission (SE) cross-sections of Ho^{3+}:YGG around 2 µm (the $^5I_7 \rightarrow {}^5I_8$ transition), denoted as σ_{SE}, were calculated using two methods with a satisfactory agreement. First, the Füchtbauer-Ladenburg (F-L) equation was used [30]:

$$\sigma_{SE}(\lambda) = \frac{\lambda^5}{8\pi\, n^2 \tau_{rad} c} \frac{W'(\lambda)}{\int \lambda W'(\lambda) d\lambda}, \tag{1}$$

where, λ denotes the wavelength, n is the refractive index at the average emission wavelength ($n = 1.91$ for YGG), c is the speed of light, τ_{rad} is the radiative lifetime of the emitting state ($^5I_7$), and $W'(\lambda)$ is the luminescence spectrum calibrated for the spectral response of the set-up and the structured water vapor absorption. The luminescence of Ho^{3+} ions was excited by focusing the radiation of a GaSb laser diode emitting at 1928nm at the polished crystal edge to reduce the effect of reabsorption and collected at 90° angle relative to the excitation direction using a home-made objective, an optical fiber and an optical spectrum analyzer (OSA, Yokogawa model AQ6375B) having a resolution of 1 nm.

Alternatively, the reciprocity method (RM) was employed, also known as the McCumber equation [31]:

$$\sigma_{SE}(\lambda) = \sigma_{abs}(\lambda) \frac{Z_1}{Z_2} exp\left(-\frac{\frac{hc}{\lambda} - E_{ZPL}}{kT}\right). \tag{2}$$

Here, h stands for the Planck constant, (hc/λ) represents the photon energy, k denotes the Boltzmann constant, T is the crystal temperature (RT), E_{ZPL} is the energy of the zero-phonon line (ZPL) transition between the lowest-lying Stark sub-levels of the two multiplets involved in the

Optics EXPRESS

transition, and Z_m are the partition functions of the lower ($m = 1$) and upper ($m = 2$) manifolds:

$$Z_m = \sum_k g_k^m exp(-E_k^m/kT). \quad (3)$$

In the given formula, g_k^m are the degeneracies of crystal-field sub-levels characterized by the index k and energy E_k^m. This energy is measured relative to the lowest sub-level within each multiplet. The crystal-field splitting for Ho^{3+} ions in YGG was taken from [32]. A comparison of the obtained SE cross-section spectra calculated by means of the F-L equation and RM is presented in Fig. 7(a). Both approaches converge by using a value of the radiative lifetime τ_{rad} of 10.3 ± 0.5 ms.

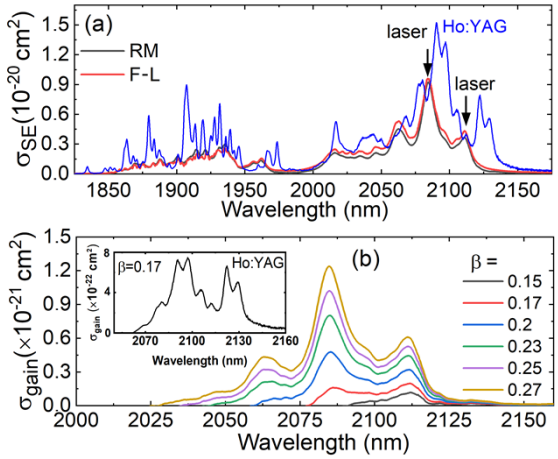

Fig. 7. Emission properties of Ho^{3+}:YGG at 2 µm (the $^5I_7 \rightarrow {}^5I_8$ transition): (a) stimulated-emission (SE), σ_{SE}, cross-sections, F-L: Füchtbauer–Ladenburg equation, RM: reciprocity method, *arrows* – observed laser wavelengths. The σ_{SE} spectrum for Ho:YAG is added for comparison. (b) gain cross-sections, $\sigma_{gain} = \beta\sigma_{SE} - (1 - \beta)\sigma_{abs}$, β – inversion ratio. Inset: gain cross sections of Ho:YAG for $\beta = 0.17$.

For the $^5I_7 \rightarrow {}^5I_8$ Ho^{3+} transition, relevant for laser operation slightly above 2 µm, the SE cross-section reaches a maximum value of 9.5×10^{-21} cm^2 at 2084nm (emission bandwidth: 17 nm). There are two additional peaks: one occurring at 2111 nm with $\sigma_{SE} = 4.3\times 10^{-21}$ cm^2, and the other at 2061nm, with $\sigma_{SE} = 5.2 \times 10^{-21}$ cm^2, as determined via the F-L formula. The calculated maximum σ_{SE} for Ho^{3+} ions in YGG is somewhat lower than that reported for Ho:YAG crystal (1.34×10^{-20} cm^2 at 2091nm) but the emission band is less structured compared to Ho:YAG, see Fig. 7(a).

Ho-lasers at 2 µm act in a quasi-three-level configuration, where gain cross-sections, given by $\sigma_{gain} = \beta\sigma_{SE}$ - (1 - β)σ_{abs}, are derived to predict possible laser wavelengths and the prospects for wavelength turning and ultrashort pulse generation. Here, $\beta = N_2(^5I_7)/N_{Ho}$ is the population inversion ratio. The calculated gain curves are illustrated in Fig. 7(b). For a modest β value of 0.15, the gain spectrum displays smooth features, ranging from 2090 to 2120 nm, with a maximum at 2111 nm. The FWHM of the gain curve is approximately 11 nm for $\beta = 0.2$. The weaker structuring of the cross sections of Ho:YGG compared to Ho:YAG manifested here is advantageous for ultrafast lasers where typical inversion rates β are of the same order of magnitude (inset Fig. 7(b)). As the population inversion ratio increases, a broad peak at ~2085nm becomes dominant in the spectra. Further increase of the inversion rate results in an additional peak emerging at 2062nm.

For the luminescence decay measurement, we employed a continuous-wave 1928-nm GaSb laser diode as an excitation source, modulating its emission with a mechanical chopper. To

Optics EXPRESS

study the luminescence dynamics, we employed the same optical spectrum analyzer working in a dynamic regime for detection at 2084nm with a 2 GHz digital oscilloscope (Tektronix, model DPO5204B). The luminescence was collected from the edge of the sample to reduce the reabsorption effect. The luminescence decay curve from the $^5I_7$ level of the Ho^{3+} ion is shown in Fig. 8. The decay is close to a single exponential one, yielding a luminescence lifetime τ_{lum} of ~8.9 ms. This is in line with a single site for Ho^{3+} ions in the YGG crystal structure. The observed lifetime is longer than that for Ho^{3+} ions in other garnet crystals, such as the disordered CNGG (7.75 ms [33]) and YAG (7.04 ms [34]).

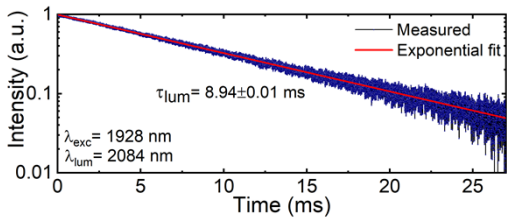

Fig. 8. Luminescence decay curve from the $^5I_7$ manifold of Ho^{3+}:YGG, λ_{exc} = 1928 nm, λ_{lum} = 2084 nm.

4. Laser operation

4.1. Laser setup

The configuration of the laser setup is illustrated in Fig. 9. A cubic laser element was cut from the as-grown 2.86 at.% Ho:YGG crystal for light propagation along the [111] direction, having an aperture of 3×3 mm^2 and a thickness of 3 mm. Both surfaces were polished to laser-grade quality with good parallelism. The uncoated crystal was mounted in a passively cooled copper holder using indium foil with thermal contact on all four lateral surfaces. A plane-concave laser cavity was employed with a radius of curvature (RoC) of 50 mm for the output coupler (OC). The flat pump mirror (PM) was coated for high transmission (HT) at the pump wavelength and high reflectance (HR) at 2.05–2.43 µm. OCs with transmission (T_{OC}) in the range 0.5% - 5% at the laser wavelength were used which were HT for the pump. The laser element was placed near the PM leaving a small airgap of less than 1 mm. The total cavity length was 49 mm.

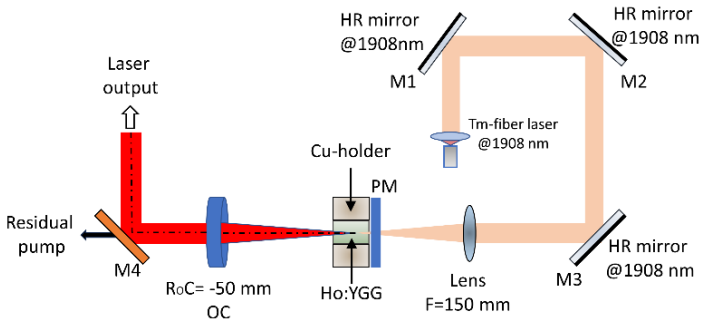

Fig. 9. Scheme of the Ho-laser setup: M1, M2 and M3 – highly-reflective mirrors for the pump radiation, M4 – dichroic mirror, PM – pump mirror, OC – output coupler.

A commercially available CW Tm-fiber laser (IPG, model TLR-5) was employed as a pump source, delivering up to 5.2 W of unpolarized output with a beam quality factor (M^2) of 1.06 at a central wavelength of 1908nm (emission bandwidth: 0.2 nm). The collimated pump beam was

Optics EXPRESS

focused into the laser crystal through the PM using an antireflection-coated spherical focusing lens with a focal length f of 150 mm. The beam radii in the focus were 16.1 μm × 38.9 μm in the sagittal and tangential planes, respectively. To capture the laser emission spectra, a spectrometer (WaveScan, APE GmbH, spectral resolution: 0.5 nm) was employed. The laser emission was separated from the residual pump using a dichroic mirror (M4) providing high reflectivity (HR, $R > 99.8\%$) at 2.05–2.16 μm and HT at 1.88–1.95 nm for 45° angle of incidence.

4.2. Laser performance

The input-output performance of the in-band pumped Ho:YGG laser is presented in Fig. 10(a). Under non-lasing conditions, the intrinsic single-pass pump absorption of the crystal was ~59% at maximum pump level, just below the calculated small-signal absorption of 62%. Thus, the ground-state bleaching was almost negligible, and under lasing conditions, the pump absorption would weakly depend on the output coupling or the pump level. The Ho:YGG laser delivered a maximum output power of 976 mW with a slope efficiency η of 50.1% with respect to the absorbed pump power and a laser threshold P_{th} of 150 mW, when using a 5% OC. The laser emission was unpolarized. The optical efficiency versus the incident pump power was 27.1%. This is much higher than the 13.5% slope efficiency reported with the same T_{OC} in [23] by using the co-doped Tm,Ho:YGG. No thermal roll-over in the output dependences was observed. The output power exhibited a linear dependence on the pump power, indicating the potential for further power scaling. By increasing the output coupling, the laser threshold gradually increased from 73 mW ($T_{OC} = 0.5\%$) to 150 mW ($T_{OC} = 5\%$).

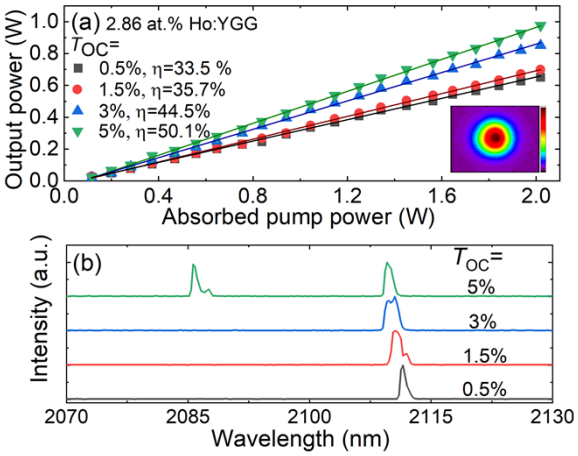

Fig. 10. Continuous-wave 2.86 at.% Ho:YGG laser pumped by a Tm-fiber laser at 1908 nm, Inset: 2D spatial intensity profile captured at a distance of 40 cm from the OC. (a) Input-output dependences, η - slope efficiency; (b) typical laser emission spectra (unpolarized output).

We used a simple model of a quasi-4-level laser with reabsorption at the laser wavelength [20] to predict the output performance of the developed in-band pumped Ho:YGG laser based on the spectroscopic parameters reported in this work. This simulation yielded an estimate for the round-trip passive losses L of 4.0 ± 0.5% and suggested a significant contribution of ETU from the upper laser level to the experimental laser threshold.

The free-running emission spectra of the Ho-laser were recorded for all output couplers at the maximum absorbed pump power, Fig. 10(b). The laser wavelength experienced a small blue shift with the output coupler transmission determined by the changing reabsorption effect in dependence on the steady-state inversion as expected for 2-μm Holmium lasers. When using a

Optics EXPRESS

low T_{OC} of 0.5%, the laser emitted at 2111 nm. However, when the OC transmission reached 5%, two laser lines simultaneously appeared at 2085 and 2109 nm, in line with the gain spectra of Ho^{3+} ions in YGG.

A circular beam profile was recorded using a Pyrocam PY-III-C-B camera (Ophir-Spiricon) at the maximum absorbed power with $T_{OC} = 5\%$, see inset Fig. 10(a).

Figure 11 presented the crystal-field splitting of the upper ($^5I_7$) and lower ($^5I_8$) laser levels of Ho^{3+} ions in the YGG crystal for the 2-μm laser transition, after Gruber *et al.* [32]. In the D2 symmetry crystal field, each $^{2S+1}L_J$ manifold with integer J is split into $2J + 1$ sub-levels numbered as 0, 1, ... 16 for $^5I_8$ and 0', 1', ... 14 for $^5I_7$. On this energy-level scheme, we indicate the pump and laser transitions for the developed in-band pumped Ho:YGG laser: 0 → 4' (pump) and 0' → 14 (laser). Barnes *et al.* proposed a criterion for distinguishing 3-level and 4-level operation schemes for lasers with reabsorption at the laser wavelength [35], namely introducing a parameter $\gamma = 1 + N_l/N_u$, where $N_l(N_u)$ are the fractional thermal populations of the lower and upper laser sub-levels, respectively. For the considered laser transition in Ho:YGG, one finds $N_l = 0.013$ and $N_u = 0.104$ at room temperature, yielding $\gamma = 1.127$ ($\gamma = 1.0$ and 2.0 for 4-level and 3-level lasers, respectively). Thus, we conclude that the developed laser operates closer to the 4-level scheme with a relatively weak effect of reabsorption at the laser wavelength.

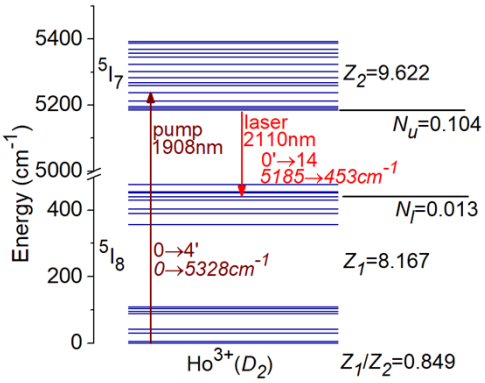

Fig. 11. Crystal-field splitting of the $^5I_8$ and $^5I_7$ manifolds of Ho^{3+} ions in D_2 sites in the YGG crystal (after [32]) showing the pump and laser transitions for the developed in-band pumped 2-μm laser, $Z_{1(2)}$ are the partition functions at room temperature, $N_l(N_u)$ are the fractional thermal populations of the lower and upper laser sub-levels, respectively, also at room temperature.

5. Conclusion

To conclude, we report on a comprehensive study of a novel material for laser operation at 2.1-μm, Holmium-doped yttrium gallium garnet. A Ho^{3+}-doped YGG crystal has been successfully grown by the optical floating zone method. The crystallographic structure has been refined, the electronic structure simulated, and Raman and optical spectroscopy performed including measuring the fluorescence lifetime. In comparison with the state-of-the-art Ho:YAG crystal, Ho:YGG exhibits stronger homogeneous line broadening in the absorption and stimulated-emission spectra around 2 μm, leading to a somewhat broader gain bandwidth. In connection with the smoother gain cross section compared to Ho:YAG, Ho:YGG is more advantageous with respect to shortest pulse generation. Furthermore, Ho:YGG exhibits a longer luminescence lifetime of the upper laser manifold, $^5I_7$, supporting low-threshold laser behavior. The latter is assigned to the difference in the crystal-field strength and the phonon spectra for Al- and Ga-based garnets. We also have demonstrated the first laser operation of Ho^{3+}:YGG on the main Ho transition delivering watt-level

Optics EXPRESS

output near 2 µm. A slope efficiency as high as 50.1% was achieved under in-band pumping at 1908nm. Further improvement of the laser performance towards high-power operation should involve a Ho^{3+} concentration-dependent study of YGG crystals, including thermal characteristics, and quantification of ETU from the upper laser manifold which is responsible for increased laser thresholds and heat loading.

Funding. Departament d'Empresa i Coneixement, Generalitat de Catalunya (2022FI_B200021); Ministerio de Ciencia, Innovación y Universidades (Project PID2022-141499OB-100).

Acknowledgment. Xavier Mateos acknowledges the Serra Húnter program.

Disclosures. The authors declare no conflicts of interest.

Data availability. Data underlying the results presented in this paper are not publicly available at this time but may be obtained from the authors upon reasonable request.

References

1. N. Sugimoto, K. Chan, N. Sims, *et al.*, "Eye-safe 2.1-µm Ho lidar for measuring atmospheric density profiles," Opt. Lett. **15**(6), 302–304 (1990).
2. S. Ishii, H. Iwai, H. Fukuoka, *et al.*, "2 µm Doppler wind lidar with a Tm:fiber-laser-pumped Ho:YLF laser," Opt. Lett. **43**(2), 202–205 (2018).
3. M. Griesbeck, H. Büker, H. Büker, *et al.*, "Mid-infrared optical parametric oscillator pumped by a high-pulse-energy, Q-switched Ho^{3+}:YAG laser," Appl. Opt. **60**(22), F21–F26 (2021).
4. E. P. Chicklis, C. A. Miller, P. A. Budni, *et al.*, "Efficient mid-infrared laser using 1.9-µm-pumped Ho:YAG and $ZnGeP_2$ optical parametric oscillators," J. Opt. Soc. Am. B **17**(5), 723–728 (2000).
5. V. Petrov, "Frequency down-conversion of solid-state laser sources to the mid-infrared spectral range using non-oxide nonlinear crystals," Prog. Quantum Electron. **42**, 1–106 (2015).
6. M. Hoffmann, S. Tomilov, J. Heidrich, *et al.*, "50-W average power Ho:YAG SESAM-modelocked thin-disk oscillator at at 2.1 µm," Opt. Express **30**(15), 27662–27673 (2022).
7. Y. Wang, P. Loiko, Y. Zhao, *et al.*, "Polarized spectroscopy and SESAM mode-locking of Tm,Ho:CALGO," Opt. Express **30**(5), 7883–7893 (2022).
8. Z. Pan, P. Loiko, Y. Wang, *et al.*, "Disordered Tm^{3+},Ho^{3+}-codoped CNGG garnet crystal: Towards efficient laser materials for ultrashort pulse generation at ~2 µm," J. Alloys Compd. **853**, 157100 (2021).
9. S. Lamrini, P. Koopmann, M. Schäfer, *et al.*, "Efficient high-power Ho:YAG laser directly in-band pumped by a GaSb-based laser diode stack at 1.9 µm," Appl. Phys. B **106**(2), 315–319 (2012).
10. G.-L. Zhu, W. Wang, B.-Q. Yao, *et al.*, "103 W in-band dual-end-pumped Ho:YAG laser," Opt. Lett. **37**(17), 3558–3560 (2012).
11. F. Díaz, N. Kuleshov, U. Griebner, *et al.*, "In-band-pumped Ho:$KLu(WO_4)_2$ microchip laser with 84% slope efficiency," Opt. Lett. **40**(3), 344–347 (2015).
12. E. D. Filer, N. P. Barnes, and B. M. Walsh, "Ho:Ho upconversion: applications to Ho lasers," J. Opt. Soc. Am. B **20**(6), 1212–1219 (2003).
13. T. Zhao, H. Chen, D. Shen, *et al.*, "Effects of Ho^{3+-}doping concentration on the performances of resonantly pumped Ho:YAG ceramic lasers," Opt. Mater. (Amsterdam, Neth.) **35**(4), 712–714 (2013).
14. B. M. Walsh, G. W. Grew, and N. P. Barnes, "Energy levels and intensity parameters of Ho^{3+} ions in $Y_3Al_5O_{12}$ and $Lu_3Al_5O_{12}$," J. Phys. Chem. Solids **67**(7), 1567–1582 (2006).
15. X. Mateos, K. Yumashev, J. Li, *et al.*, "Passive Q-switching of microchip lasers based on Ho:YAG ceramics," Appl. Opt. **55**(18), 4877–4887 (2016).
16. L. Esterowitz and R. C. Stoneman, "Intracavity-pumped 2.09-µm Ho:YAG laser," Opt. Lett. **17**(10), 736–738 (1992).
17. D. Y. Shen, A. Abdolvand, L. J. Cooper, *et al.*, "Efficient Ho: YAG laser pumped by a cladding-pumped tunable Tm: Silica-fibre laser," Appl. Phys. B **79**(5), 559–561 (2004).
18. J. Zhang, F. Schulze, K. F. Mak, *et al.*, "High-power, high-efficiency Tm:YAG and Ho:YAG thin-disk lasers," Laser Photon. Rev. **12**(3), 1700273 (2018).
19. M. Rupp, M. Eichhorn, and C. Kieleck, "Iterative 3D modeling of thermal effects in end-pumped continuous-wave Ho^{3+}:YAG lasers," Appl. Phys. B **129**(1), 4–11 (2023).
20. T. Mocek, X. Mateos, J. M. Serres, *et al.*, "Microchip laser operation of Yb-doped gallium garnets," Opt. Mater. Express **6**(1), 46–57 (2016).
21. H. Yu, K. Wu, B. Yao, *et al.*, "Growth and characteristics of Yb-doped $Y_3Ga_5O_{12}$ laser crystal," IEEE J. Quantum Electron. **46**(12), 1689–1695 (2010).
22. Q. Li, F. Wang, F. Liang, *et al.*, "Diode-pumped mid-infrared Tm:YGG laser at 2.0 and 2.3 µm," Opt. Laser Technol. **168**, 109961 (2024).
23. C. Quan, D. Sun, H. Zhang, *et al.*, "7.25 W LD side-pumped Er:YGG CW laser operated at 2.8 µm," Appl. Phys. B **129**(11), 184 (2023).
24. L. F. Johnson, J. F. Dillon, and J. P. Remeika, "Optical properties of Ho^{3+} Ions in yttrium gallium garnet and yttrium iron garnet," Phys. Rev. B **1**(5), 1935–1946 (1970).

Optics EXPRESS

25. Y. Yang and X. Cheng, "Investigations on a new laser medium of 2 μm: Tm^{3+}, Ho^{3+} co-doped $Y_3Ga_5O_{12}$ crystal," Russ. J. Inorg. Chem. **67**(S2), S169–S176 (2022).
26. L. F. Johnson and G. J. Dixon, "Low-threshold 2-μm holmium laser excited by nonradiative energy transfer from Fe^{3+} in YGG," Opt. Lett. **17**(24), 1782–1784 (1992).
27. S. Fu, J. Tan, X. Bai, *et al.*, "Effect of Al/Ga substitution on the structural and luminescence properties of $Y_3(Al_{1-x}Ga_x)_5O_{12}$: Ce^{3+} phosphors," Opt. Mater. **75**, 619–625 (2018).
28. Z. Pan, X. Mateos, J. M. Serres, *et al.*, "Comparative study of the spectroscopic and laser properties of Tm^{3+}, $Na^+(Li^+)$-codoped $Ca_3Nb_{1.5}Ga_{3.5}O_{12}$-type disordered garnet crystals for mode-locked lasers," Opt. Mater. Express **8**(8), 2287–2299 (2018).
29. V. Monteseguro, P. Rodríguez-Hernández, R. Vilaplana, *et al.*, "Lattice dynamics study of nanocrystalline yttrium gallium garnet at high pressure," J. Phys. Chem. C **118**(24), 13177–13185 (2014).
30. B. F. Aull and H. P. Jenssen, "Vibronic interactions in Nd: YAG resulting in nonreciprocity of absorption and stimulated emission cross sections," IEEE J. Quantum Electron. **18**(5), 925–930 (1982).
31. S. A. Payne, L. L. Chase, L. K. Smith, *et al.*, "Infrared cross-section measurements for crystals doped with Er^{3+}, Tm^{3+}, and Ho^{3+}," IEEE J. Quantum Electron. **28**(11), 2619–2630 (1992).
32. J. B. Gruber, G. W. Burdick, U. V. Valiev, *et al.*, "Energy levels and symmetry assignments for Stark components of Ho^{3+} ($4f^{10}$) in yttrium gallium garnet ($Y_3Ga_5O_{12}$)," J. Appl. Phys. **106**(11), 113110 (2009).
33. D. Li, J. Xu, N. Li, *et al.*, "Spectral properties and laser performance of Ho:CNGG crystals grown by the micro-pulling-down method," Opt. Mater. Express **9**(6), 2490–2496 (2019).
34. P. Loiko, L. Basyrova, R. Maksimov, *et al.*, "Comparative study of Ho:Y_2O_3 and Ho:$Y_3Al_5O_{12}$ transparent ceramics produced from laser-ablated nanoparticles," J. Lumin. **240**, 118460 (2021).
35. N. P. Barnes, B. M. Walsh, R. L. Hutcheson, *et al.*, "Pulsed $^4F_{3/2}$ to $^4I_{9/2}$ operation of Nd lasers," J. Opt. Soc. Am. B **16**(12), 2169–2177 (1999).